Original Research

Dynamic Contrast-Enhanced Magnetic Resonance Imaging of Human Melanoma Xenografts With Necrotic Regions

Jon-Vidar Gaustad, MSc, Ilana C. Benjaminsen, MSc, Else-Beate M. Ruud, MSc, and Einar K. Rofstad, PhD*

Purpose: To investigate whether high-resolution images of necrotic regions in tumors can be derived from gadopentetate dimeglumine (Gd-DTPA)-based dynamic contrast-enhanced magnetic resonance imaging (DCE-MRI) series.

Materials and Methods: E-13 human melanoma xenografts were used as preclinical models of human cancer. DCE-MRI was performed at a voxel size of $0.23 \times 0.47 \times 2.0$ mm^3 with the use of spoiled gradient recalled sequences. Tumor images of $E \cdot F$ (E is the initial extraction fraction of Gd-DTPA and F is blood perfusion) and λ (the partition coefficient of Gd-DTPA, which is proportional to extracellular volume fraction) were produced by subjecting DCE-MRI series to Kety analysis, and these images were compared with histological preparations from the imaged slices.

Results: Strong correlations were found between fraction of necrotic tissue and fraction of voxels with $\lambda > \lambda_L$ for λ_L values of 0.4 to 0.6. Binary λ images differentiating between λ values $> \lambda_L$ and λ values $< \lambda_L$ were found to mirror necrotic regions well in tumors with large necroses. However, necrotic foci that were small compared with the voxel size were not detectable.

Conclusion: Clinically relevant images of necrotic tumor regions can be obtained for E-13 melanomas by subjecting Gd-DTPA-based DCE-MRI series to Kety analysis.

Key Words: DCE-MRI; Kety analysis; melanoma xenografts; blood perfusion; hypoxia; necrosis; extracellular volume fraction
J. Magn. Reson. Imaging 2007;26:133–143.

MALIGNANT TUMORS develop a physiological microenvironment during growth that is distinctly different from that of normal tissues (1). The microenvironment of tumors is heterogeneous due to inadequate blood perfusion and is characterized by oxygen and nutrient depletion, low energy status, extracellular acidosis, and interstitial hypertension (2). This hostile microenvironment causes resistance to therapy (3) and may promote malignant progression and metastatic dissemination (4).

Gadopentetate dimeglumine (Gd-DTPA)-based dynamic contrast-enhanced magnetic resonance imaging (DCE-MRI) has been suggested to be a useful noninvasive method for characterizing the physiological microenvironment of tumors (5–10). The uptake of Gd-DTPA in tumor tissue depends on several microenvironmental parameters, including blood perfusion, vascular density, vessel wall permeability, cell density, extracellular volume fraction, and extracellular matrix density (11). In some types of cancer, correlations have been found between DCE-MRI-derived parameters and physiological parameters of the tumor microenvironment (7–10) or outcome of tumor treatment (12–14). However, the correlations are in general weak, implying that the DCE-MRI parameters derived from these studies have low prognostic or predictive value.

The potential usefulness of Gd-DTPA-based DCE-MRI in providing high-resolution images of tumor blood perfusion and tumor oxygenation status is currently being investigated in our laboratory by using human tumor xenografts as preclinical models of human cancer (15–19). We have shown that highly reproducible, high-resolution images of $E \cdot F$ (E is the initial extraction fraction of Gd-DTPA and F is blood perfusion) and λ (λ is the partition coefficient of Gd-DTPA, which is proportional to extracellular volume fraction) can be obtained by subjecting DCE-MRI series to Kety analysis (15). The $E \cdot F$ and λ images were found to mirror the histological appearance of the tumor tissue. Thus, $E \cdot F$ was positively correlated to microvascular density, and λ was positively correlated to extracellular volume fraction (15–17). Moreover, the $E \cdot F$ images were shown to mirror blood perfusion images assessed by using the Bioscope imaging system to measure the uptake of freely

Group of Radiation Biology and Tumor Physiology, Department of Radiation Biology, Institute for Cancer Research, The Norwegian Radium Hospital, Oslo, Norway.

*Address reprint requests to: E.K.R., PhD, Department of Radiation Biology, Institute for Cancer Research, The Norwegian Radium Hospital, Montebello, N-0310 Oslo, Norway.
E-mail: e.k.rofstad@labmed.uio.no

Grant sponsor: Norwegian Cancer Society.

Received August 12, 2006; Accepted January 15, 2007.

DOI 10.1002/jmri.20939
Published online in Wiley InterScience (www.interscience.wiley.com).

diffusible radioactive blood flow tracers (18), and strong correlations were found between $E \cdot F$ and fraction of radiobiologically hypoxic cells assessed by using a radiobiological assay based on the paired survival curve method (19). These studies were carried out with A-07 and/or R-18 human melanomas transplanted into BALB/c-*nu*/*nu* mice (15–19), primarily because xenografted tumors of these melanoma lines do not develop necrotic regions during growth (20). Experimental tumors without necrosis are particularly suitable for evaluating the potential of DCE-MRI in providing clinically useful images of the physiological microenvironment of tumors because the premises of the pharmacokinetic models developed for analysis of DCE-MRI data are not fulfilled in necrotic tumor regions (11).

However, development of necrotic regions is a characteristic feature of many tumor types. Histological examinations have shown that the pattern of necrosis can differ substantially among individual tumors resected from the same organ. Some tumors show a few large necrotic regions centrally that may differ significantly in size and shape whereas others develop many small necrotic foci throughout the tissue. Immunohistochemical investigations of tumors labeled with hypoxia markers have revealed that most necrotic regions are circumscribed by a thin layer of hypoxic cells, usually two to four cell layers thick (21). These hypoxic cells are resistant to radiation therapy, photodynamic therapy, and some forms of chemotherapy and may thus represent a serious therapeutic problem, particularly if they are reoxygenated because of therapy-induced changes in the diffusion distances of oxygen (1–3). Necrotic tumor regions do not represent a therapeutic problem but may confound DCE-MRI-derived physiological images because the pharmacokinetic models developed for analyzing DCE-MRI data are not valid for necrotic tissue (11). Values provided for voxels in necrotic tissue by pharmacokinetic models have no physiological meaning but may be similar to those provided for hypoxic tissue or poorly perfused normoxic tissue (15,17,18) and, if so, tumors with necrotic regions may be assessed to be more poorly perfused or more hypoxic than they actually are. The main purpose of the work reported here was to investigate whether necrotic regions can be identified in $E \cdot F$ and/or λ images of experimental tumors. $E \cdot F$ and λ images were achieved by subjecting DCE-MRI series of E-13 human melanoma xenografts to Kety analysis, and these images were compared with histological preparations from the imaged tumor cross sections. The E-13 melanoma was selected for this study because individual tumors of this line develop highly different necrotic patterns and thus differ substantially in fraction of necrotic tissue.

MATERIALS AND METHODS

Mice and Tumors

Adult (8–12 weeks of age) female BALB/c-*nu*/*nu* mice, bred at our research institute, were used as host animals for xenografted tumors. The mice were kept under specific pathogen-free conditions at constant temperature (24–26°C) and humidity (30–50%). Sterilized food and tap water were given ad libitum. Animal care and experimental procedures were approved by the Institutional Committee on Research Animal Care and were performed in accordance with the Interdisciplinary Principles and Guidelines for the Use of Animals in Research, Marketing, and Education (New York Academy of Sciences, New York, NY, USA).

The experiments were performed with tumors of the amelanotic human melanoma E-13. This melanoma was established in BALB/c-*nu*/*nu* mice from a lymph node metastasis of a 52-year-old female. It has been maintained by serial subcutaneous transplantation in athymic mice. The tumors used in the experiments reported here were initiated from cell suspensions prepared from donor tumors by mechanical and enzymatic disaggregation (22). Approximately 3.0×10^5 cells in 10 μL of Ca^{2+}-free and Mg^{2+}-free Hanks' balanced salt solution were inoculated intradermally into the mouse flank by using a 100-μL Hamilton syringe. The tumors were subjected to DCE-MRI upon having grown to volumes of 200 to 350 mm^3. Tumor volume (V) was calculated as $V = (\pi/6)ab^2$, where a is the longer and b is the shorter of two perpendicular diameters (23), measured with calipers.

Immunohistochemical Detection of Tumor Hypoxia

Pimonidazole was used as a marker of tumor hypoxia, and a peroxidase-based immunohistochemical assay was used to detect hypoxic regions in tumors (24). Pimonidazole hydrochloride, kindly supplied by Professor J.A. Raleigh (Department of Radiation Oncology, University of North Carolina School of Medicine, Chapel Hill, NC, USA), was dissolved in 0.9% NaCl and administered intraperitoneally (i.p.) in doses of 30 mg/kg body weight. The tumors were dissected free from the mice approximately four hours after the administration of pimonidazole and fixed in phosphate-buffered 4% paraformaldehyde. Slides with tumor tissue preparations were incubated with polyclonal rabbit antiserum to pimonidazole–protein adducts, a gift from Professor J.A. Raleigh. Diaminobenzidine was used as chromogen, and hematoxylin was used for counterstaining. Hypoxic fractions (HFs) (i.e., area fractions showing positive pimonidazole staining) and necrotic fractions (NFs) (i.e., area fractions showing necrotic tissue) were determined by image analysis.

Anesthesia

DCE-MRI was carried out with anesthetized mice. Fentanyl citrate/fluanisone (Janssen Pharmaceutica, Beerse, Belgium) and midazolam (Hoffmann-La Roche, Basel, Switzerland) were administered i.p. in doses of 0.63/20 and 10 mg/kg body weight, respectively.

Contrast Agent

Gd-DTPA (Schering, Berlin, Germany), diluted in 0.9% saline to a final concentration of 0.06 M, was used as contrast agent. The contrast agent was administered in the tail vein of the mice in a bolus dose of 5.0 mL/kg body weight during a period of five seconds. The admin-

istration was performed after the mice had been placed in the MR scanner by using a 24-G neoflon connected to a syringe by polyethylene tubing.

DCE-MRI

Tumor imaging was performed with a 1.5-T whole-body scanner (Signa, General Electric, Milwaukee, WI, USA), using a cylindrical slotted tube resonator transceiver coil especially constructed for mice (25). The coil was insulated with Styrofoam to prevent excessive heat loss from the mice. The body core temperature of the mice was kept at 37 to 38°C during imaging by using a thermostatically-regulated heating pad. The mice were placed in the scanner with the tumor in the isocenter. Two calibration tubes, one with 0.5 mM Gd-DTPA in 0.9% saline and the other with 0.9% saline only, were placed adjacent to the mice in the coil. The tumors were imaged axially in a single section through the tumor center. Sagittal scans were used to localize the tumor and determine the position of the axial scan. A scan thickness of 2 mm was used, and the number of excitations was 1. The image matrix was 256 × 64 with a field of view of 6 × 3 cm^2, corresponding to a voxel size of 0.23 × 0.47 × 2.0 mm^3. Interpolation algorithms applied by the imaging system resulted in an apparent resolution of 0.23 × 0.23 × 2.0 mm^3. Two types of spoiled recalled gradient images were recorded: proton density images with repetition time TR = 900 msec, echo time TE = 3.2 msec, and flip angle $\alpha = 20°$, and T_1-weighted images with TR = 200 msec, TE = 3.2 msec, and $\alpha = 80°$. Two proton density images and three T_1-weighted images were acquired before the contrast agent was administered. The durations of the sequences were 64 and 14 seconds, respectively. After the administration of contrast agent, T_1-weighted images were recorded every 14 seconds for 15 minutes. Finally, one proton density image was acquired.

Image Processing and Data Analysis

Tumor images were stored in the DICOM format and analyzed on a voxel-by-voxel basis by using software developed in IDL (Interactive Data Language, Boulder, CO, USA). Gd-DTPA concentrations were calculated from signal intensities by using the method of Hittmair et al (26). Plots of Gd-DTPA concentration vs. time were generated, and the Kety equation (27),

$$C_t(T) = E \cdot F \cdot \int_0^T C_a(t) \cdot e^{-E \cdot F \cdot (T-t)/\lambda}\, dt, \qquad (1)$$

was fitted to the plots, where $C_t(T)$ is the Gd-DTPA concentration in the tumor at time T, E is the initial extraction fraction of Gd-DTPA, F is the perfusion per unit tumor volume, $C_a(t)$ is the arterial input function, and λ is the partition coefficient of Gd-DTPA. The arterial input function has been determined previously (15):

$$C_a(t) = A \cdot e^{-B \cdot t} + C \cdot e^{-D \cdot t}, \qquad (2)$$

where A = 2.55 mM, B = 0.080 $second^{-1}$, C = 1.20 mM, and D = 0.0010 $second^{-1}$. Numerical values of λ and $E \cdot F$ were determined for each voxel from the best curve fit. $E \cdot F$ was calculated in units of mL/(g · minute), assuming that the density of the tumor tissue was 1 g/cm^3 = 1 g/mL. Images of λ and $E \cdot F$ were generated by using the SigmaPlot software (SPSS Science, Chicago, IL, USA).

Statistical Analysis

Correlations between two parameters were searched for by linear regression analysis. Probability values (P) and correlation coefficients (R) were calculated by using the SigmaStat statistical software (SPSS Science, Chicago, IL, USA). A significance criterion of $P < 0.05$ was used.

RESULTS

A total of 20 tumors were subjected to DCE-MRI and subsequent histological examination. Histologically, the tumors showed a chorded structure, that is, the tumors were built up by cylindrical tissue structures with a vessel in the center (Fig. 1). The chords were separated by necrotic tissue in tumor regions with low vascular density. The cells in the periphery of the chords stained positive for pimonidazole and were thus hypoxic. In tumor regions with high vascular density, the chords overlapped and individual chords could not be easily identified. Pimonidazole-positive hypoxic cells were barely seen in these regions. Some tumors developed regions with massive necrosis centrally. The intertumor heterogeneity in NF and HF was substantial. This is illustrated in Fig. 1, which shows histological preparations from the central axial plane (i.e., from the center of the 2-mm-thick axial DCE-MRI scan) of four of the 20 tumors. Some tumors showed little necrosis and a few hypoxic foci (Fig. 1a), some tumors showed little necrosis and extensive hypoxia (Fig. 1b), some tumors showed massive central necrosis and extensive hypoxia (Fig. 1c), and some tumors showed massive central necrosis and a few hypoxic foci (Fig. 1d).

The intratumor heterogeneity in NF and HF was also significant. In fact, the histological appearance of the tissue differed substantially within the 2-mm-thick tumor slices subjected to DCE-MRI. This is illustrated in Fig. 2, which shows six 5-μm-thick histological preparations from the imaged slice of a single, representative tumor. The histological preparations were separated by ~400 μm, and they show that the pimonidazole staining pattern and the size, shape, and spatial location of the massive central necrosis changed considerably within a distance of ~2 mm. Consequently, to determine representative values for NF and HF of imaged slices, six histological sections were prepared from each slice. These histological preparations were analyzed separately, mean values were calculated for NF and HF, and these mean values were compared with $E \cdot F$ and λ values determined by DCE-MRI.

Tumors with extensive necrosis showed lower $E \cdot F$ values and higher λ values than tumors with little necrosis. This is illustrated in Figs. 3 and 4, which refer to a tumor with massive central necrosis and a tumor with

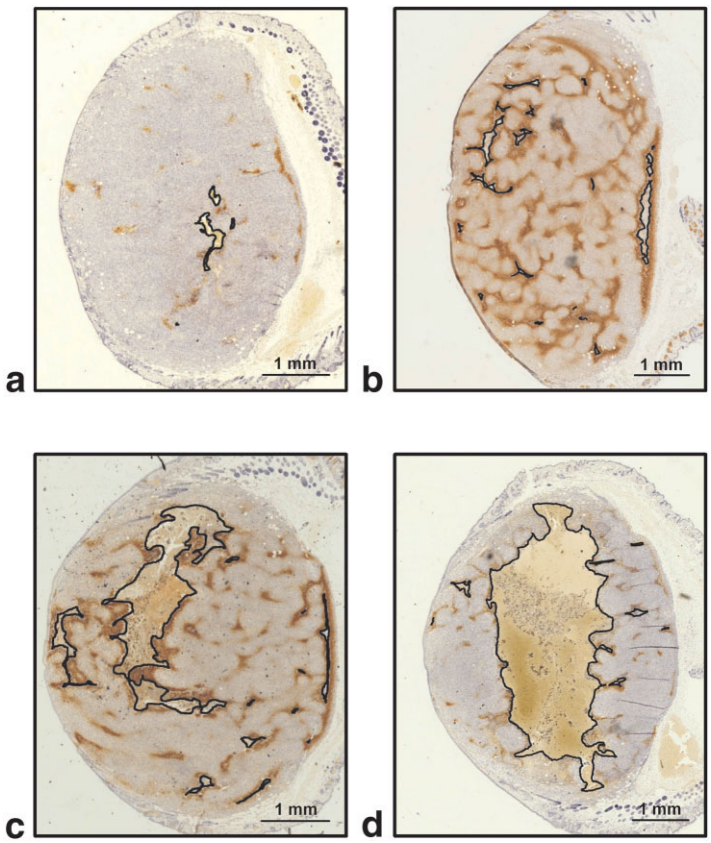

Figure 1. Intertumor heterogeneity in NF and HF. Histological preparations from the central axial plane of four E-13 tumors, illustrating the intertumor heterogeneity in histological appearance. The images refer to the center of the 2-mm-thick DCE-MRI scan of a tumor showing little necrosis and a few hypoxic foci (**a**), a tumor showing little necrosis and extensive hypoxia (**b**), a tumor showing massive central necrosis and extensive hypoxia (**c**), and a tumor showing massive central necrosis and a few hypoxic foci (**d**). The preparations were stained with anti-pimonidazole antibody to visualize hypoxic regions and counterstained with hematoxylin. Hypoxic tissue appears dark brown. Necrotic regions are outlined in black.

a few small necrotic foci, respectively. The figures show a histological preparation from the center of the axial DCE-MRI scan (Figs. 3a and 4a), a sketch in which the necrotic regions in each of the six histological preparations from the scanned slice have been outlined (Figs. 3b and 4b), the $E \cdot F$ image (Figs. 3c and 4c), the λ image (Figs. 3d and 4d), the frequency distribution of the $E \cdot F$ values (Figs. 3e and 4e), and the frequency distribution of the λ values (Figs. 3f and 4f). Our algorithms produced relatively low $E \cdot F$ values [$E \cdot F < 0.03$ mL/(g $\cdot$ minute)] for most voxels in tumor regions with massive necrosis. A significant fraction of the voxels in normoxic tumor regions without necrosis also showed low $E \cdot F$ values, implying that low $E \cdot F$ values were not a distinctive feature of necrotic tissue. Consequently, large necrotic regions were poorly defined and small necrotic foci could not be identified in $E \cdot F$ images of E-13 tumors (Figs. 3c and 4c). Moreover, our algorithms pro-

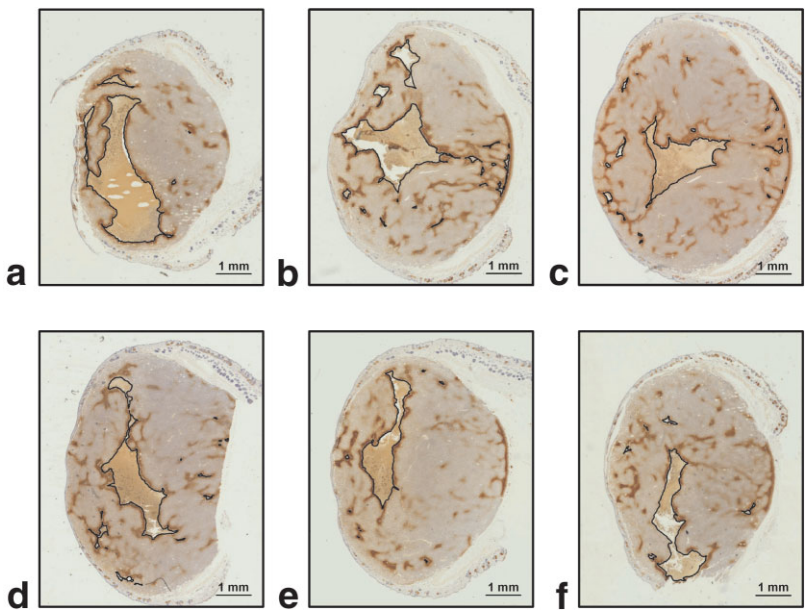

Figure 2. Intratumor heterogeneity in NF and HF. Six histological preparations from the central axial plane of a single E-13 tumor, illustrating the intratumor heterogeneity in histological appearance within a distance of ~2 mm, corresponding to the thickness of the DCE-MRI scans. The images refer to 5-μm-thick parallel sections separated by ~400 μm from the cranial (**a**) to the caudal (**f**) end of the tumor. The preparations were stained with anti-pimonidazole antibody to visualize hypoxic regions and counterstained with hematoxylin. Hypoxic tissue appears dark brown. Necrotic regions are outlined in black.

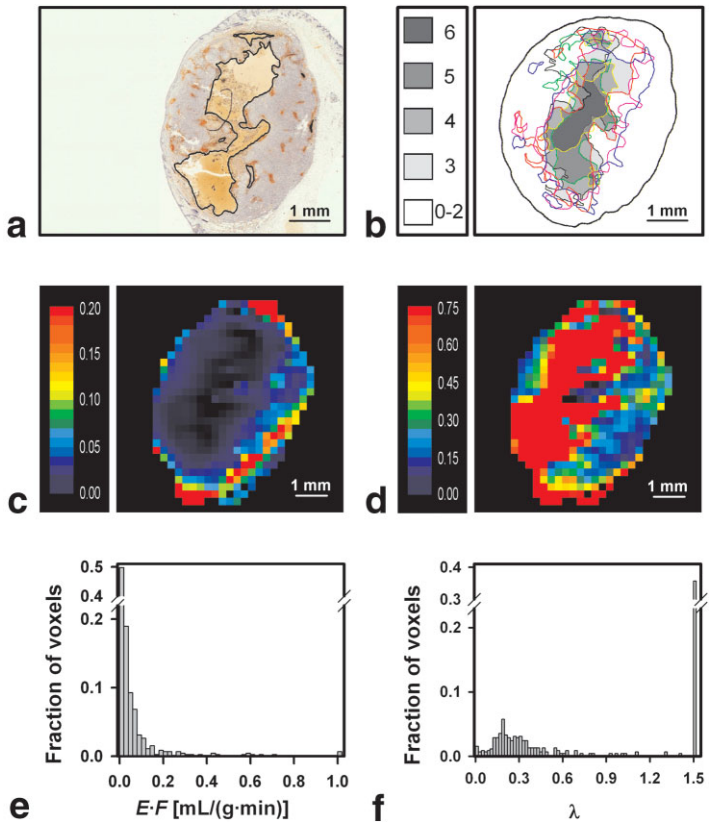

Figure 3. E-13 tumor with extensive necrosis. A histological preparation from the center of the axial DCE-MRI scan (**a**), a sketch in which the necrotic regions in each of the six histological sections prepared from the scanned slice have been outlined (**b**), the $E \cdot F$ image (**c**), the λ image (**d**), the frequency distribution of the $E \cdot F$ values (**e**), and the frequency distribution of the λ values (**f**) of an E-13 tumor with massive central necrosis. a: The histological preparation was stained with anti-pimonidazole antibody to visualize hypoxic regions and counterstained with hematoxylin. Hypoxic tissue appears dark brown. Necrotic regions are outlined in black. b: The necrotic regions in each of the six histological preparations are outlined in individual colors and superimposed. The gray shade indicates the number of preparations with overlapping necrotic tissue. The scale is given by the bar. c,d: The $E \cdot F$ and λ scales are given by the color bars. e,f: The $E \cdot F$ and λ frequency distributions are based on the individual voxel values of the imaged slice. The median values of $E \cdot F$ and λ were found to be 0.02 mL/(g · minute) and 0.47, respectively.

duced very high λ values (λ >> 1) for most voxels in tumor regions with massive necrosis, whereas λ values >0.7 were rarely seen for voxels in normoxic tumor regions without necrosis. Large necrotic regions could, therefore, be recognized as regions with very high λ values in λ images of E-13 tumors (Fig. 3d). However, small necrotic foci were not detectable in the λ images of tumors of this line (Fig. 4d).

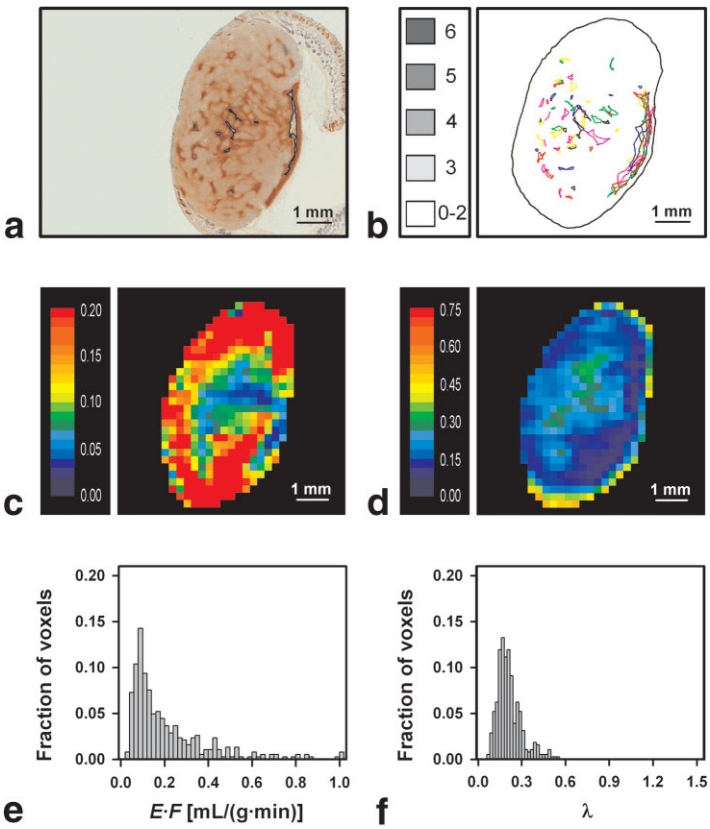

Figure 4. E-13 tumor with little necrosis. A histological preparation from the center of the axial DCE-MRI scan (**a**), a sketch in which the necrotic regions in each of the six histological sections prepared from the scanned slice have been outlined (**b**), the $E \cdot F$ image (**c**), the λ image (**d**), the frequency distribution of the $E \cdot F$ values (**e**), and the frequency distribution of the λ values (**f**) of an E-13 tumor with a few small necrotic foci. a: The histological preparation was stained with anti-pimonidazole antibody to visualize hypoxic regions and counterstained with hematoxylin. Hypoxic tissue appears dark brown. Necrotic regions are outlined in black. b: The necrotic regions in each of the six histological preparations are outlined in individual colors and superimposed. The gray shade indicates the number of preparations with overlapping necrotic tissue. The scale is given by the bar. c,d: The $E \cdot F$ and λ scales are given by the color bars. e,f: The $E \cdot F$ and λ frequency distributions are based on the individual voxel values of the imaged slice. The median values of $E \cdot F$ and λ were found to be 0.14 mL/(g · minute) and 0.20, respectively.

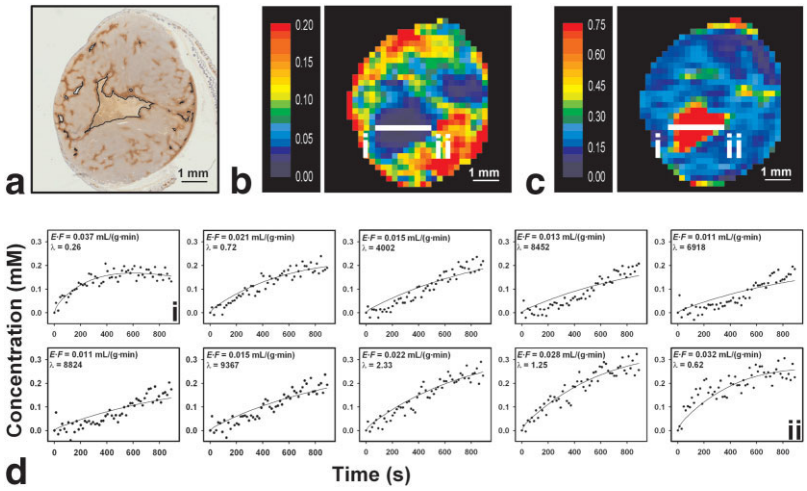

Figure 5. Kety curves for voxels in necrotic tumor regions. A histological preparation from the center of the axial DCE-MRI scan (**a**), the $E \cdot F$ image (**b**), the λ image (**c**), and plots of Gd-DTPA concentration vs. time and the corresponding Kety curves for 10 individual voxels (**d**) of an E-13 tumor with a large central necrosis. a: The histological preparation was stained with anti-pimonidazole antibody to visualize hypoxic regions and counterstained with hematoxylin. Hypoxic tissue appears dark brown. Necrotic regions are outlined in black. b,c: The $E \cdot F$ and λ scales are given by the color bars. The median values of $E \cdot F$ and λ for the imaged slice were found to be 0.09 mL/(g · minute) and 0.20, respectively. d: The Kety curves refer to single subsequent voxels form *i* to *ii* along the 10-voxel-long white bar depicted in (b) and (c). The voxel bar crosses the central necrosis in (a). The $E \cdot F$ and λ values of each voxel along the voxel bar are presented in (d).

The impact of necrosis on $E \cdot F$ and λ was studied further by subjecting individual voxels adjacent to or within necrotic tumor regions to detailed analysis. One representative example referring to a tumor with a large central necrosis is illustrated in Fig. 5. The figure shows a histological preparation from the axial DCE-MRI scan (Fig. 5a), the $E \cdot F$ image (Fig. 5b), the λ image (Fig. 5c), and Kety curves for ten individual voxels (Fig. 5d). The Kety curves refer to the voxels of the ten-voxel-long white bar depicted in Figs. 5b and c. The voxel bar crosses the necrotic region, and the Kety curves represent subsequent voxels from *i* to *ii*. Examination of the six histological sections prepared from the tumor revealed that the voxels along the white bar consisted of a mixture of necrotic tissue and hypoxic and normoxic nonnecrotic tissue. The first two and the last three voxels were dominated by nonnecrotic tissue. The Kety analysis produced $E \cdot F$ values of 0.021–0.037 mL/(g · minute) and λ values of 0.26–2.33 for these voxels. The remaining five voxels were dominated by necrotic tissue. The data for these voxels were consistent with a linear increase in Gd-DTPA concentration with time. When the data were subjected to Kety analysis, $E \cdot F$ values ≤ 0.015 mL/(g · minute) and λ values $>1 \times 10^3$ were produced by our algorithms. It should be noticed that the Kety analysis produced poor curve fits for these voxels.

To investigate whether the intertumor heterogeneity in λ reflected the intertumor heterogeneity in NF and/or NF + HF, several parameters were derived from the λ frequency distributions of the 20 tumors included in our study, including the 20th, 30th, 40th, 50th, 60th, 70th, and 80th percentiles and the fraction of voxels with $\lambda > \lambda_L$ (λ_L is λ_{Limit}, a threshold value for λ) for λ_L values of 0.2, 0.3, 0.4, 0.5, 0.6, 0.7, 0.8, 0.9, and 1.0. Linear regression analysis revealed that these percentiles correlated weakly with NF and NF + HF and that fraction of voxels with $\lambda > \lambda_L$ correlated strongly with NF and NF + HF. The strongest correlations are illustrated in Figs. 6 and 7, which show fraction of voxels with $\lambda > 0.4$ vs. NF (Fig. 6a: $R^2 = 0.41$, $P = 0.0023$), fraction of voxels with $\lambda > 0.5$ vs. NF (Fig. 6b: $R^2 = 0.47$, $P = 0.00082$), fraction of voxels with $\lambda > 0.6$ vs. NF (Fig. 6c: $R^2 = 0.48$, $P = 0.00069$), fraction of voxels with $\lambda > 0.7$ vs. NF (Fig. 6d: $R^2 = 0.48$, $P = 0.00074$), fraction of voxels with $\lambda > 0.3$ vs. NF + HF (Fig. 7a: $R^2 = 0.53$, $P = 0.00026$), fraction of voxels with $\lambda > 0.4$ vs. NF + HF (Fig. 7b: $R^2 = 0.55$, $P = 0.00018$), fraction of voxels with $\lambda > 0.5$ vs. NF + HF (Fig. 7c: $R^2 = 0.55$, $P = 0.00020$), and fraction of voxels with $\lambda > 0.6$ vs. NF + HF (Fig. 7d: $R^2 = 0.52$, $P = 0.00031$). It should be noticed that the fraction of voxels with $\lambda > \lambda_L$ for λ_L values of 0.3 to 0.6 usually was larger than NF + HF for tumors with extensive necrosis and smaller than NF + HF for tumors with little necrosis (Fig. 7).

Voxels with $\lambda > \lambda_L$ for λ_L values of 0.4 of 0.6 colocalized with the regions with necrotic or hypoxic tissue in tumors with extensive necrosis whereas tumors with little necrosis hardly showed voxels with λ values >0.4. This is illustrated in Figs. 8 and 9 by using the tumors depicted in Figs. 3 and 4 as examples. Figure 8 refers to a tumor with massive central necrosis and Fig. 9 to a tumor with a few small necrotic foci. The figures show a histological preparation from the center of the axial DCE-MRI scan (Figs. 8a and 9a), a sketch in which the necrotic regions in each of the six histological preparations from the scanned slice have been outlined (Figs. 8b and 9b), a sketch in which the regions with either necrotic or hypoxic tissue in each of the six histological preparations from the scanned slice have been outlined (Figs. 8c and 9c), a λ image highlighting voxels with $\lambda > 0.6$

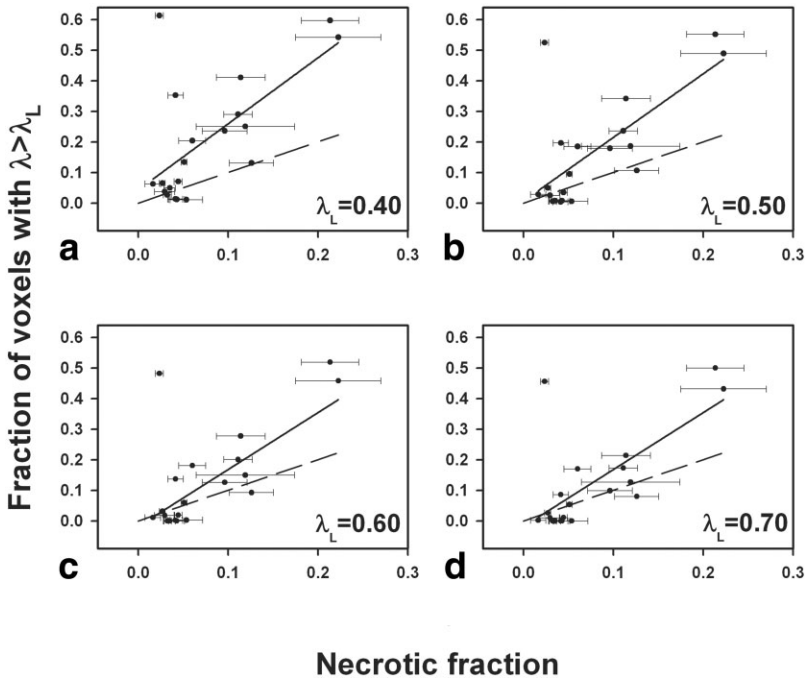

Figure 6. Relationship between λ and NF. Fraction of voxels with λ > 0.4 (**a**), λ > 0.5 (**b**), λ > 0.6 (**c**), and λ > 0.7 (**d**) vs. necrotic fraction for 20 E-13 tumors. Data points represent individual tumors. Horizontal bars indicate SEs, calculated from six histological preparations. The solid lines represent curves fitted to the data by linear regression analysis. The correlations were found to be statistically significant: (a) $R^2 = 0.41$, $P = 0.0023$; (b) $R^2 = 0.47$, $P = 0.00082$; (c) $R^2 = 0.48$, $P = 0.00069$; and (d) $R^2 = 0.48$; $P = 0.00074$. The dashed lines represent the one-to-one correlations.

(Figs. 8d and 9d), a λ image highlighting voxels with λ > 0.5 (Figs. 8e and 9e), and a λ image highlighting voxels with λ > 0.4 (Figs. 8f and 9f). Generally, binary λ images similar to those in Figs. 8d–f and 9d–f were found to give an adequate impression of the location of the necrotic tissue in tumors with large necroses, whereas small necrotic foci could not be detected.

Moreover, to investigate whether the intertumor heterogeneity in $E \cdot F$ reflected the intertumor heterogeneity in NF and/or NF + HF, several parameters were derived from the $E \cdot F$ frequency distributions of the tumors, including the 20th, 30th, 40th, 50th, 60th, 70th, and 80th percentiles and the fraction of voxels with $E \cdot F < E \cdot F_L$ ($E \cdot F_L$ is $E \cdot F_{Limit}$, a threshold value for $E \cdot F$) for $E \cdot F_L$ values of 0.10, 0.08, 0.06, 0.04, 0.02, and 0.01 mL/(g · minute). Correlations between these $E \cdot F$ parameters and NF or NF + HF were then searched for by linear regression analysis. Only weak correlations were found, regardless of the $E \cdot F$ parameter considered (data not shown). Similarly, to investigate whether a combination of $E \cdot F$ and λ parameters reflected the intertumor heterogeneity in NF and/or NF + HF, correlations between the fraction of voxels having both λ > λ_L and $E \cdot F < E \cdot F_L$ and NF or NF + HF were searched

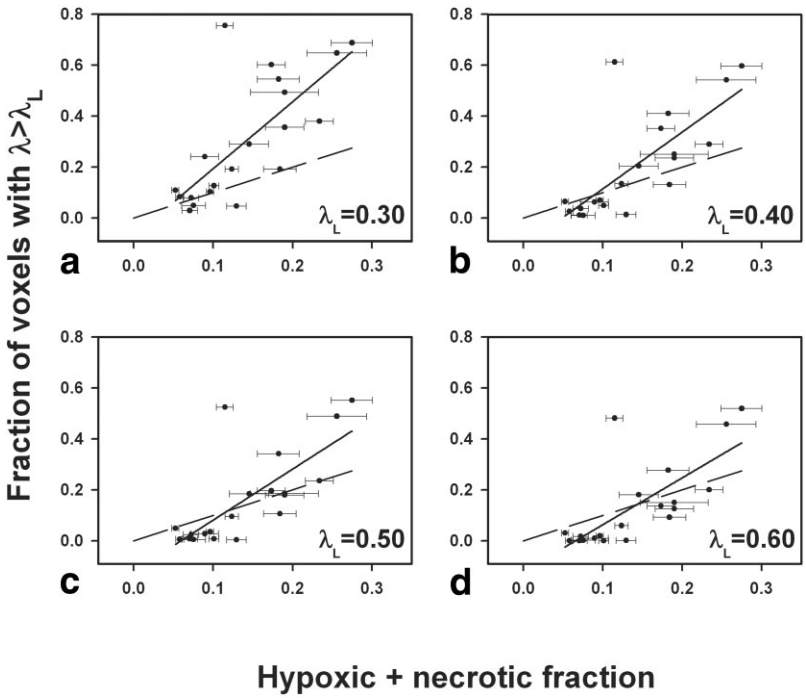

Figure 7. Relationship between λ and NF + HF. Fraction of voxels with λ > 0.3 (**a**), λ > 0.4 (**b**), λ > 0.5 (**c**), and λ > 0.6 (**d**) vs. the sum of the hypoxic and necrotic fraction for 20 E-13 tumors. Data points represent individual tumors. Horizontal bars indicate SEs, calculated from six histological preparations. The solid lines represent curves fitted to the data by linear regression analysis. The correlations were found to be statistically significant: (a) $R^2 = 0.53$, $P = 0.00026$; (b) $R^2 = 0.55$, $P = 0.00018$; (c) $R^2 = 0.55$, $P = 0.00020$; (d) $R^2 = 0.52$, $P = 0.00031$. The dashed lines represent the one-to-one correlations.

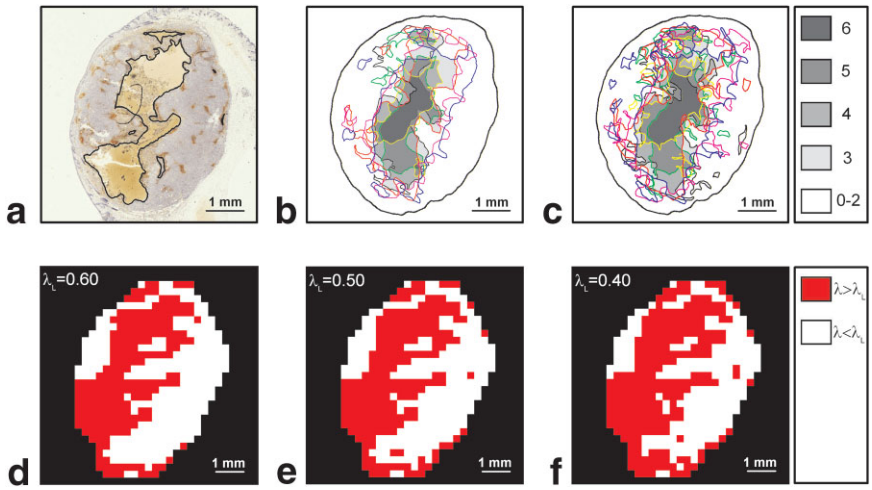

Figure 8. Binary λ images of E-13 tumor with massive necrosis. A histological preparation from the center of the axial DCE-MRI scan (**a**), a sketch in which the necrotic regions in each of the six histological sections prepared from the scanned slice have been outlined (**b**), a sketch in which the largest regions with either hypoxic or necrotic tissue in each of the six histological sections prepared from the scanned slice have been outlined (**c**), a λ image highlighting voxels with $\lambda > 0.6$ (**d**), a λ image highlighting voxels with $\lambda > 0.5$ (**e**), and a λ image highlighting voxels with $\lambda > 0.4$ (**f**) of an E-13 tumor with massive central necrosis. a: The histological preparation was stained with anti-pimonidazole antibody to visualize hypoxic regions and counterstained with hematoxylin. Hypoxic tissue appears dark brown. Necrotic regions are outlined in black. b,c: The necrotic regions (b) and the regions with either hypoxic or necrotic tissue (c) in each of the six histological preparations are outlined in individual colors and superimposed. The gray shade indicates the number of preparations with overlapping necrotic tissue (b) or overlapping regions with either hypoxic or necrotic tissue (c). The scale is given by the bar. d–f: Voxels with $\lambda > 0.6$ (d), $\lambda > 0.5$ (e), and $\lambda > 0.4$ (f) are indicated in red.

for by using all possible combinations of the λ_L and $E \cdot F_L$ values stated above. However, these correlations were weaker than those obtained by using fraction of voxels with $\lambda > \lambda_L$ as parameter (data not shown), implying that the λ frequency distributions provided significant information on NF and NF + HF in E-13 tumors and that the $E \cdot F$ frequency distributions did not provide additional information.

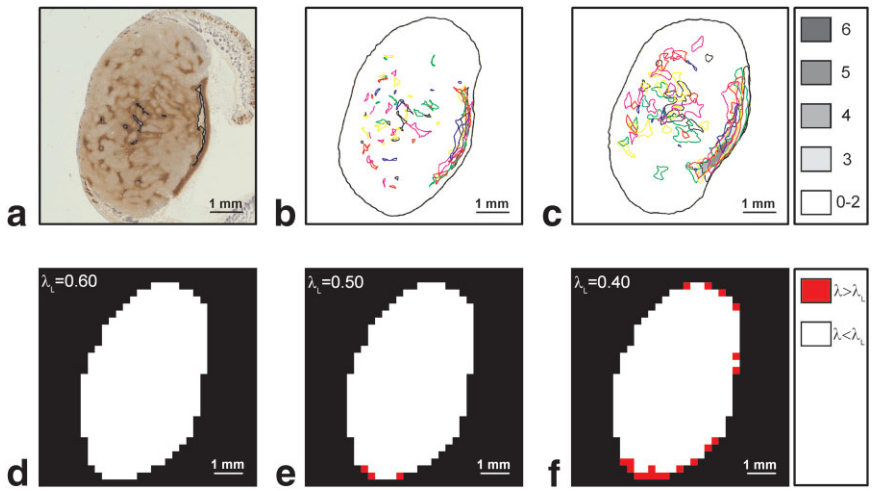

Figure 9. Binary λ images of E-13 tumor with small necrotic foci. A histological preparation from the center of the axial DCE-MRI scan (**a**), a sketch in which the necrotic regions in each of the six histological sections prepared from the scanned slice have been outlined (**b**), a sketch in which the largest regions with either hypoxic or necrotic tissue in each of the six histological sections prepared from the scanned slice have been outlined (**c**), a λ image highlighting voxels with $\lambda > 0.6$ (**d**), a λ image highlighting voxels with $\lambda > 0.5$ (**e**), and a λ image highlighting voxels with $\lambda > 0.4$ (**f**) of an E-13 tumor with a few small necrotic foci. a: The histological preparation was stained with anti-pimonidazole antibody to visualize hypoxic regions and counterstained with hematoxylin. Hypoxic tissue appears dark brown. Necrotic regions are outlined in black. b,c: The necrotic regions (b) and the regions with either hypoxic or necrotic tissue (c) in each of the six histological preparations are outlined in individual colors and superimposed. The gray shade indicates the number of preparations with overlapping necrotic tissue (b) or overlapping regions with either hypoxic or necrotic tissue (c). The scale is given by the bar. d–f: Voxels with $\lambda > 0.6$ (d), $\lambda > 0.5$ (e), and $\lambda > 0.4$ (f) are indicated in red.

DISCUSSION

Tumors with poor blood perfusion and low oxygen tension are resistant to some types of chemotherapy, photodynamic therapy, and radiation therapy (1–3). A noninvasive method for identifying tumors that are resistant to treatment because of an unfavorable physiological microenvironment is, therefore, highly needed. Several experimental and clinical studies have suggested that DCE-MRI may be developed to be a clinically useful method for assessing tumor responsiveness to treatment. Thus, in some studies, tumor parameters derived by DCE-MRI have been shown to correlate with outcome of treatment as well as with physiological parameters of the tumor microenvironment assessed by invasive methods (7–14). However, the correlations are in general weak, possibly because the complex and heterogeneous microenvironment of tumors may complicate the interpretation of DCE-MRI-derived physiological images. A large number of tumors develop necroses in regions with poor blood perfusion and low oxygen tension, and because of poor contrast enhancement, necrotic regions may appear like poorly perfused tissue in DCE-MRI-derived physiological images of tumors. If necrotic tissue is misinterpreted as hypoxic tissue or poorly perfused normoxic tissue, DCE-MRI-derived physiological images may suggest that tumors with necrotic regions have larger regions with hypoxic or poorly perfused viable tissue than they actually have. The possibility that clinically useful images of necrotic regions in tumors may be achieved by appropriate analysis of DCE-MRI series was investigated in the study reported here.

Xenografted tumors of the E-13 human melanoma were used as preclinical models of tumors in humans in our study, primarily because the intra- and intertumor heterogeneity in NF and HF is particularly large in E-13 tumors. Some tumors showed little necrosis and a few hypoxic foci, some tumors showed little necrosis and extensive hypoxia, some tumors showed massive central necrosis and extensive hypoxia, and some tumors showed massive central necrosis and a few hypoxic foci. Moreover, the histological appearance of the tumors differed substantially within the 2-mm-thick slices subjected to DCE-MRI. Consequently, E-13 tumors should be excellent models for testing the hypothesis put forward in our study.

Several pharmacokinetic models are being used for estimating physiological parameters from DCE-MRI data of tumors (28). Studies in our laboratory have shown that the Kety model (27) is a useful pharmacokinetic model for analyzing images obtained by Gd-DTPA-based DCE-MRI of amelanotic human melanoma xenografts (15–19). The Kety model is based on the assumption that the transvascular flux of contrast agent is limited purely by the blood flow (27). This assumption has been verified to be valid for our melanoma xenografts (15,18), implying that E is close to unity and $E \cdot F$ gives absolute values of tumor blood perfusion in units of mL/(g · minute). Moreover, our Kety analysis is based on the assumption that the uptake of Gd-DTPA is limited by the size of the extracellular space (15,19). This assumption has also been shown to be valid for nonnecrotic tissue in our melanoma xenografts, implying that λ is proportional to the extracellular volume fraction (18,19). However, the latter assumption is not valid for necrotic tumor regions (18).

Proper Kety analysis requires Gd-DTPA concentration-vs.-time curves with a well-defined maximum (11,27). In the E-13 tumors studied here, the concentration of Gd-DTPA increased nearly linearly with time in voxels consisting primarily of necrotic tissue. This means that the diffusion of Gd-DTPA into the voxels was higher than the diffusion of Gd-DTPA out of the voxels during the whole observation period of 15 minutes, primarily because the uptake of Gd-DTPA was not limited by the size of the extracellular space in the necrotic tissue. Therefore, the Kety equation gave poor fits to the Gd-DTPA concentration-vs.-time curves of these voxels (i.e., the Kety model broke down in tumor regions with extensive necrosis). However, when the Gd-DTPA uptake data for necrotic voxels were subjected to Kety analysis, our algorithms produced extremely low values for $E \cdot F$ and extremely high values for λ. Our study was based on the hypothesis that these $E \cdot F$ and λ values might be utilized to produce detailed images of necrotic regions in tumor tissue. It should be noticed, however, that $E \cdot F$ and λ values produced by subjecting necrotic tissue to Kety analysis have no physiological meaning. It is thus possible that necrotic regions in tumors also may be identified by model-independent semiquantitative analyses of Gd-DTPA concentration-vs.-time curves.

Our hypothesis was found to be valid for λ but not for $E \cdot F$. The Kety analysis indeed produced low $E \cdot F$ values for most voxels in tumor regions with massive necrosis. However, low $E \cdot F$ values were not a distinctive feature of necrotic tissue. Some tumor regions consisting exclusively of nonnecrotic tissue also showed low $E \cdot F$ values within the same range as those produced for necrotic tissue. Consequently, only weak correlations were found between fraction of voxels with $E \cdot F < E \cdot F_L$ for $E \cdot F_L$ values within the range of 0.01–0.10 mL/(g · minute) and NF or NF + HF, and even large massive necroses were not well defined in $E \cdot F$ images of poorly perfused tumors.

On the other hand, fraction of voxels with $\lambda > \lambda_L$ for λ_L values within the range of 0.4 to 0.6 was found to correlate strongly with NF and NF + HF, and voxels with λ values $> \lambda_L$ colocalized with necrotic regions in tumors with extensive necrosis. Interestingly, fraction of voxels with $\lambda > \lambda_L$ correlated better with NF + HF than with NF independent of the λ_L value (λ_L = 0.4–0.6), probably because most of the hypoxic tissue was seen as thin bands of hypoxic cells located adjacent to necrotic tissue. Voxel values of λ within the same range as those produced for necrotic tissue were not seen in tumor regions consisting exclusively of nonnecrotic tissue. Consequently, binary λ images differentiating between λ values $> \lambda_L$ and λ values $< \lambda_L$ (λ_L = 0.4–0.6) were found to mirror necrotic regions well in tumors with large necroses. However, the size of the necrotic regions was slightly overestimated in these images, probably because the voxels in the periphery of large necroses consisted of a mixture of necrotic and nonne-

crotic tissue, and because of the necrotic component, λ values $> \lambda_L$ were produced for many of these voxels. In tumors with little necrosis, the fraction of voxels with $\lambda > \lambda_L$ was usually smaller than NF and NF + HF, probably because the necrotic regions in these tumors were small compared with the voxel size of $0.23 \times 0.47 \times 2.0$ mm^3. Therefore, the voxels of tumors with small necrotic regions consisted of nonnecrotic tissue only or a significant fraction of nonnecrotic tissue and a smaller fraction of necrotic tissue. The λ values produced for the latter voxels were within the same range as those produced for the voxels consisting of nonnecrotic tissue only and, consequently, small necrotic foci were not detectable in binary λ images differentiating between λ values $> \lambda_L$ and λ values $< \lambda_L$ ($\lambda_L = 0.4–0.6$). However, by reducing the scan thickness to less than 2 mm, it should be possible to detect smaller necrotic regions than those detected here, provided that a sufficiently high signal-to-noise ratio can be achieved. Moreover, an increased spatial resolution would probably also improve the delineation of large necrotic regions in binary λ images.

Our preclinical study thus strongly suggests that images of necrotic regions in tumors may be derived from DCE-MRI data by subjecting the data to appropriate analysis. Furthermore, the size of the necrotic regions that can be detected appears to be limited primarily by the spatial resolution of the DCE-MRI. Most importantly, binary λ images may mirror necrotic regions well in tumors with large necroses. This observation may have significant clinical implications. Several institutions are attempting to develop prognostic parameters as well as predictive assays for the outcome of treatment of cancer patients based on DCE-MRI (7–14). Moreover, DCE-MRI is being used extensively to monitor the response to treatment of cancer patients (29–31). The prognostic value of DCE-MRI and its usefulness in prediction and monitoring of tumor treatment response may be improved substantially by implementing adequate methods for differentiating between necrotic tissue and poorly perfused hypoxic or normoxic tissue. The present study suggests that λ images produced by subjecting DCE-MRI data to Kety analysis may be used successfully for that purpose, at least for human tumors with biological characteristics similar to those of E-13 tumors, a possibility that merits clinical investigation. Furthermore, the possibility that our observation may be of general validity should be investigated thoroughly in preclinical and clinical studies involving tumors with widely different biological characteristics.

REFERENCES

1. Vaupel P. Tumor microenvironmental physiology and its implication for radiation oncology. Semin Radiat Oncol 2004;14:198–206.
2. Vaupel P, Kallinowski F, Okunieff P. Blood flow, oxygen and nutrient supply, and metabolic microenvironment of human tumors: a review. Cancer Res 1989;49:6449–6465.
3. Brown JM, Giaccia AJ. The unique physiology of solid tumors: opportunities (and problems) for cancer therapy. Cancer Res 1998; 58:1408–1416.
4. Rofstad EK. Microenvironment-induced cancer metastasis. Int J Radiat Biol 2000;76:589–605.
5. Buckley DL, Drew PJ, Mussurakis S, Monson JR, Horsman A. Microvessel density of invasive breast cancer assessed by dynamic Gd-DTPA enhanced MRI. J Magn Reson Imaging 1997;7:461–464.
6. Hawighorst H, Knapstein PG, Knopp MV, et al. Uterine cervical carcinoma: comparison of standard and pharmacokinetic analysis of time-intensity curves for assessment of tumor angiogenesis and patient survival. Cancer Res 1998;58:3598–3602.
7. Lyng H, Vorren AO, Sundfør K, Lien HH, Kaalhus O, Rofstad EK. Intra- and intertumor heterogeneity in blood perfusion of human cervical cancer before treatment and after radiotherapy. Int J Cancer 2001;96:182–190.
8. Lyng H, Vorren AO, Sundfør K, Lien HH, Kaalhus O, Rofstad EK. Assessment of tumor oxygenation in human cervical carcinoma by use of dynamic Gd-DTPA-enhanced MR imaging. J Magn Reson Imaging 2001;14:750–756.
9. Cooper RA, Carrington BM, Loncaster JA, et al. Tumour oxygenation levels correlate with dynamic contrast-enhanced magnetic resonance imaging parameters in carcinoma of the cervix. Radiother Oncol 2000;57:53–59.
10. Mayr NA, Yuh WT, Arnholt JC, et al. Pixel analysis of MR perfusion imaging in predicting radiation therapy outcome in cervical cancer. J Magn Reson Imaging 2000;12:1027–1033.
11. Tofts PS. Modeling tracer kinetics in dynamic Gd-DTPA MR imaging. J Magn Reson Imaging 1997;7:91–101.
12. Yamashita Y, Baba T, Baba Y, et al. Dynamic contrast-enhanced MR imaging of uterine cervical cancer: pharmacokinetic analysis with histopathologic correlation and its importance in predicting the outcome of radiation therapy. Radiology 2000;216:803–809.
13. Loncaster JA, Carrington BM, Sykes JR, et al. Prediction of radiotherapy outcome using dynamic contrast-enhanced MRI of carcinoma of the cervix. Int J Radiat Oncol Biol Phys 2002;54:759–767.
14. de Vries AF, Kremser C, Hein PA, et al. Tumor microcirculation and diffusion predict therapy outcome for primary rectal carcinoma. Int J Radiat Oncol Biol Phys 2003;56:958–965.
15. Benjaminsen IC, Graff BA, Brurberg KG, Rofstad EK. Assessment of tumor blood perfusion by high-resolution DCE-MRI: a preclinical study of human melanoma xenografts. Magn Reson Med 2004;52: 269–276.
16. Gaustad JV, Benjaminsen IC, Graff BA, Brurberg KG, Ruud EBM, Rofstad EK. Intratumor heterogeneity in blood perfusion in orthotopic human melanoma xenografts assessed by dynamic contrast-enhanced magnetic resonance imaging. J Magn Reson Imaging 2005;21:792–800.
17. Graff BA, Benjaminsen IC, Melås EA, Brurberg KG, Rofstad EK. Changes in intratumor heterogeneity in blood perfusion in intradermal human melanoma xenografts during tumor growth assessed by DCE-MRI. Magn Reson Imaging 2005;23:961–966.
18. Graff BA, Benjaminsen IC, Brurberg KG, Ruud EBM, Rofstad EK. Comparison of tumor blood perfusion assessed by dynamic contrast-enhanced MRI with tumor blood supply assessed by invasive imaging. J Magn Reson Imaging 2005;21:272–281.
19. Egeland TAM, Gaustad JV, Vestvik IK, Benjaminsen IC, Mathiesen B, Rofstad EK. Assessment of fraction of radiobiologically hypoxic cells in human melanoma xenografts by dynamic contrast-enhanced MRI. Magn Reson Med 2006;55:874–882.
20. Rofstad EK. Orthotopic human melanoma xenograft model systems for studies of tumour angiogenesis, pathophysiology, treatment sensitivity and metastatic pattern. Br J Cancer 1994;70:804–812.
21. Raleigh JA, Chou SC, Bono EL, Thrall DE, Varia MA. Semiquantitative immunohistochemical analysis for hypoxia in human tumors. Int J Radiat Oncol Biol Phys 2001;49:569–574.
22. Rofstad EK, Henriksen K, Galappathi K, Mathiesen B. Antiangiogenic treatment with thrombospondin-1 enhances primary tumor radiation response and prevents growth of dormant pulmonary micrometastases after curative radiation therapy in human melanoma xenografts. Cancer Res 2003;63:4055–4061.
23. Steel GG. Growth rate of tumours. In: Steel GG, editor. Growth kinetics of tumours. Oxford: Clarendon Press; 1977. p 5–7.
24. Rofstad EK, Måseide K. Radiobiological and immunohistochemical assessment of hypoxia in human melanoma xenografts: acute and chronic hypoxia in individual tumours. Int J Radiat Biol 1999;75: 1377–1393.

25. Rofstad EK, Steinsland E, Kaalhus O, Chang YB, Høvik B, Lyng H. Magnetic resonance imaging of human melanoma xenografts in vivo: proton spin-lattice and spin-spin relaxation times versus fractional tumour water content and fraction of necrotic tumour tissue. Int J Radiat Biol 1994;65:387–401.
26. Hittmair K, Gomiscek G, Langenberger K, Recht M, Imhof H, Kramer J. Method for the quantitative assessment of contrast agent uptake in dynamic contrast-enhanced MRI. Magn Reson Med 1994;31:567–571.
27. Kety S. Theory of blood-tissue exchange and its application to measurements of blood flow. Methods Med Res 1960;8:228–236.
28. Tofts PS, Brix G, Buckley DL, et al. Estimating kinetic parameters from dynamic contrast-enhanced T_1-weighted MRI of a diffusable tracer: standardized quantities and symbols. J Magn Reson Imaging 1999;10:223–232.
29. Knopp MV, Giesel FL, Marcos H, von Tengg-Kobligk H, Choyke P. Dynamic contrast-enhanced magnetic resonance imaging in oncology. Top Magn Reson Imaging 2001;12:301–308.
30. Montemurro F, Martincich L, de Rosa G, et al. Dynamic contrast-enhanced MRI and sonography in patients receiving primary chemotherapy for breast cancer. Eur Radiol 2005;15:1224–1233.
31. Morgan B, Utting JF, Higginson A, Thomas AL, Steward WP, Horsfield MA. A simple, reproducible method for monitoring the treatment of tumours using dynamic contrast-enhanced MR imaging. Br J Cancer 2006;94:1420–1427.